Journal of Geophysics and Engineering, 2025, **22**(5), 1378–1391
https://doi.org/10.1093/jge/gxaf081
Advance access publication date: 2025 June 30
Research Article

OXFORD

Microseismic attenuation tomography of coalbed methane hydraulic fracturing zones

Jiachen Wang[1], Haijiang Zhang[1,2,*], Jing Hu[3], and Huasheng Zha[1,4]

[1]Department of Geophysics and Planetary Sciences, School of Earth and Space Sciences, University of Science and Technology of China, Hefei 230026, China
[2]Mengcheng National Geophysical Observatory, University of Science and Technology of China, Mengcheng, Anhui 233500, China
[3]School of Geological Engineering and Geomatics, Chang'an University, Xi'an 710054, China
[4]Anhui Wantai Geophysical Technology Co. Ltd., Hefei 230601, China
*Corresponding author. No. 96, Jinzhai Road, Baohe District, Hefei City, 230041, Anhui Province, China. E-mail: zhang11@ustc.edu.cn

Abstract

Hydraulic fracturing is widely applied for efficient coalbed methane (CBM) extraction, with microseismic monitoring providing critical insights into the spatial distribution of fracturing zones. However, using only microseismic event locations may bias fracturing zone characterization, as some areas can be aseismic. In this study, to better delineate fracturing zones, we use seismic attenuation anomalies by conducting microseismic attenuation tomography. This study utilizes microseismic waveform data associated with two hydraulic fracturing wells for the CBM extraction in a coal mine in Shanxi, China. First, the amplitude spectra of the P- and S-wave waveforms are used to determine t^*, a path attenuation parameter that represents the cumulative attenuation along the ray paths between events and stations and is related to the quality factor Q. Then, t^* values are used to invert for three-dimensional Q_p and Q_s models based on the existing velocity models and microseismic event locations, respectively. In this study, microseismic events in the fracturing zones are associated with relatively high Q values compared to the shallower zones. Based on previous laboratory studies, gas saturation zones are characterized by high Q anomalies. Therefore, we can use high Q areas around the hydraulic fracturing wells to delineate effective fracturing zones, which are also associated with low V_p and high V_s anomalies. Our study shows that microseismic attenuation tomography can be used to delineate the fracturing zones and to evaluate the gas saturation state for the case of coalbed methane hydraulic fracturing.

Keywords: microseismic monitoring; coalbed methane; hydraulic fracturing; body wave attenuation tomography; Q_p and Q_s

1. Introduction

Coalbed methane (CBM) is a type of unconventional hydrocarbon gas resource (Wang 2012). Meanwhile, high concentration of CBM is also considered a potential hazard for coal mining. Therefore, CBM needs to be properly extracted for the purpose of energy usage and safety concern. The extraction of CBM from the target coal beds depends on the permeability and gas saturation percentage, which affect the gas migration rate and the ultimate recoverability of gas in the reservoir (Moore 2012). To increase the permeability of reservoir, hydraulic fracturing has been widely used for unconventional oil/gas reservoirs (Maxwell 2014; Jiang *et al.* 2016; Han *et al.* 2021). For the hydraulic fracturing of CBM reservoir, the fracturing well spacing needs to be properly set. If the well spacing is too large, it can result in reservoir stimulation gaps between adjacent wells, leading to the waste of CBM resources and potential gas outburst risk. On the other hand, if the well spacing is too small, it can cause excessive overlap of reservoir stimulation areas and unnecessary engineering expenses. In addition, accurate delineation of effective reservoir stimulation zone is also a significant part of CBM reservoir characterization and management (Mohamed & Mehana 2020).

Hydraulic fracturing alters the pore pressure, stress, and strain conditions within rocks, leading to rock fracturing accompanied by microseismic events (Ellsworth 2013; Maxwell 2014; Blake *et al.* 2020). By monitoring microseismic events during the hydraulic fracturing process, we can effectively characterize the spatiotemporal distributions of fractures. Additionally, monitoring microseismic activity can be helpful for mitigating potential induced seismicity risks related to the activation of pre-existing faults by hydraulic fracturing, thereby ensuring the safety of production activities (Ellsworth 2013; Chen *et al.* 2017; Miao *et al.* 2019; Blake *et al.* 2020; Han *et al.* 2021; Wang *et al.* 2023; Wang *et al.* 2024).

Microseismic monitoring can be categorized into two types: downhole monitoring and surface monitoring. For surface monitoring, geophones or seismometers are deployed on the surface around the fracturing wells. It has the advantage of providing better spatial coverage for microseismic events and thus they have higher horizontal accuracy than downhole monitoring. However, it may have poorer capability of detecting weak events because microseismic signals are heavily attenuated by the soft sediments near the surface (Chambers *et al.* 2010; Eisner *et al.* 2015; Alexandrov *et al.* 2020; Yang *et al.* 2023; Mao *et al.* 2025).

Currently, microseismic monitoring relies on the microseismic event locations to characterize the distribution of the created fractures by hydraulic fracturing. However, due to the weak nature of the microseismic signals, it is not possible to identify and locate all of them (Miao *et al.* 2019). Moreover, the location accuracy is subject to uncertainties in arrival times and velocity models, which can introduce biases for characterizing the distribution of fractures solely based on the microseismic locations. In addition to microseismic locations,

Received: December 15, 2024. **Revised:** June 3, 2025. **Accepted:** June 28, 2025

seismic tomography can also be used to characterize the fracturing zones based on velocity changes due to fracturing. For example, Chen *et al.* (2017) used downhole microseismic monitoring data to image shale gas fracturing zones. Miao *et al.* (2019) used surface microseismic monitoring array to determine velocity changes caused by shale gas hydraulic fracturing. Wang *et al.* (2023) utilized surface microseismic monitoring array to characterize the coalbed methane fracturing zones based on velocity anomalies. By combining velocity anomalies and event locations, hydraulic fracturing zones can be better delineated.

Arrival-time-based seismic location and tomography methods only utilize the kinematic information of seismic waves, while neglecting their dynamic characteristics. In addition to velocity structures (V_p and V_s) obtained through the inversion of arrival times, seismic attenuation structure can be used to better delineate the existence of subsurface fractures and fluids (Dutta & Odé 1979; Toksöz *et al.* 1979; Wu *et al.* 2014; Blake *et al.* 2020).

The quality factor Q quantitatively represents the attenuation strength of the subsurface medium. Q is defined as the magnitude of energy attenuation during the propagation of seismic waves over one cycle (Knopoff 1964), with Q inversely proportional to the attenuation intensity. The observed amplitude spectrum is affected by two types of attenuation mechanism: intrinsic attenuation and scattering attenuation (Aki & Chouet 1975; Frankel 1991). Intrinsic attenuation is the phenomenon of irreversible energy dissipation of seismic waves caused by the hysteresis of the medium during wave propagation. It is mainly related to rock properties such as porosity, pore density, pore shape, and fluid/gas saturation. Previous studies, based on numerical simulations and rock physics experiments, have shown that frictional sliding on the fracture surface is the primary mechanism affecting intrinsic attenuation in fractured rocks. Especially when the fractures are partially or fully filled with fluids, elastic waves are further attenuated (Dutta & Odé 1979; Johnston *et al.* 1979; Toksöz *et al.* 1979; Peacock *et al.* 1994; Blake *et al.* 2020; Liao *et al.* 2023). On the other hand, scattering attenuation refers to the seismic wave amplitude variations caused by focusing, defocusing, and scattering during the wave propagation (Aki & Chouet 1975; Toksöz *et al.* 1979; Frankel 1991).

Various seismic attenuation tomography methods have been proposed to estimate the Q models, including ray-based 3D seismic attenuation tomography using direct waves (Scherbaum 1990; Bennington *et al.* 2008; Pozgay *et al.* 2009; Pesicek *et al.* 2011; Bisrat *et al.* 2014; Eisner *et al.* 2015; Barthwal *et al.* 2019; Blake *et al.* 2020), full waveform inversion (Tromp *et al.* 2005; Zhu *et al.* 2013; Karaoğlu & Romanowicz 2017), 2D Lg/Sg or Pn/Sn seismic attenuation (Nicolas *et al.* 1982; Campillo *et al.* 1984; Al-Damegh *et al.* 2004; Zhao & Mousavi 2018), and surface wave attenuation tomography (Dalton & Ekström 2006; Lawrence & Prieto 2011; Lin *et al.* 2012; Bowden *et al.* 2017). The ray-based methods using first-arrival P- or S-waves, which we employ in this study, estimate t^* by fitting the seismic amplitude spectrum and then invert for Q values. The primary advantages of ray-based methods include high computational efficiency, and high-resolution Q models in the region with dense ray coverage. However, they rely on an accurate velocity model for raypath calculations and do not fully account for frequency dependence or scattering effects (Aki & Chouet 1975; Scherbaum 1990; Bennington *et al.* 2008). In contrast, full waveform inversion provides high-resolution attenuation models by simulating full wave propagation, incorporating scattering and focusing effects, but requires significant computational resources and high-quality data (Tromp *et al.* 2005; Zhu *et al.* 2013; Karaoğlu & Romanowicz 2017). Regional phase attenuation tomography (e.g. using Pn, Sn, or Lg waves) is effective for studying crustal and upper mantle structures but suffers from limited depth resolution (Campillo *et al.* 1984; Al-Damegh *et al.* 2004; Zhao & Mousavi 2018). Surface wave attenuation tomography, although capable of accounting for focusing-defocusing effects, may face challenges in constraining vertical variations of deep structures, as distinct frequency components exhibit varying penetration depths (Lawrence *et al.* 2006; Lawrence & Prieto 2011; Lin *et al.* 2012).

There have been some attenuation studies applied in the geothermal development (Romero Jr *et al.* 1997; Guo & Thurber 2021) and underground coal mining (Barthwal *et al.* 2019). However, currently there are few studies on how the attenuation (Q) structure of the fracturing zone is changed compared to the surrounding medium. Therefore, by applying seismic attenuation tomography to microseismic monitoring data caused by hydraulic fracturing of CBM reservoirs, it provides a valuable opportunity to study attenuation properties of rock formations under the gas-rich environment. Similar to using seismic velocity anomalies to characterize the fracturing zone (Wang *et al.* 2023), it is also possible to use seismic attenuation anomalies to delineate the effective fracturing zone. Therefore, in this study we aim to use microseismic data monitored by the surface seismic array to determine the three-dimensional (3D) attenuation structure for the fracturing zone of coalbed methane, which is helpful for delineating the fracturing zone and understanding reservoir properties. The inversion recovers the total attenuation ($Q^{-1}_{total} = Q^{-1}_{intrinsic} + Q^{-1}_{scattering}$), and separation of the two components requires additional data analysis (e.g. coda waves; Aki & Chouet 1975).

2. Methods

One commonly used approach is first to directly invert for the path attenuation term t^* from the observed seismic amplitude spectrum using the first arrivals of P- and S-waves. Then, using ray theory, the obtained t^* values are used to perform 3D tomography of Q. By assuming a Brune source model (Brune 1970) and utilizing the high-frequency decay rate of the amplitude spectrum, t^* and other source model parameters, such as the corner frequency and the low-frequency amplitude spectrum level, can be simultaneously obtained by fitting seismic amplitude spectra for many events and stations. Once t^* values are obtained, the attenuation structure can be determined by calculating ray paths with a known 3D velocity model (Scherbaum 1990; Bennington *et al.* 2008; Pozgay *et al.* 2009; Barthwal *et al.* 2019). In the following subsections, we will briefly introduce the adopted seismic attenuation tomography method, as shown in the flowchart in Fig. 1.

2.1. Spectrum fitting and t^*

At an observation station j, the event amplitude spectrum A^{obs}_{ij} for event i can be represented as (Scherbaum 1990)

$$A^{obs}_{ij} = O_{ij}(f)\, S_j(f)\, I_j(f)\, B_{ij}(f), \quad (1)$$

where $O_{ij}(f)$, $S_j(f)$, $I_j(f)$, and $B_{ij}(f)$ represent source spectrum, site response, instrument response, and path attenua-

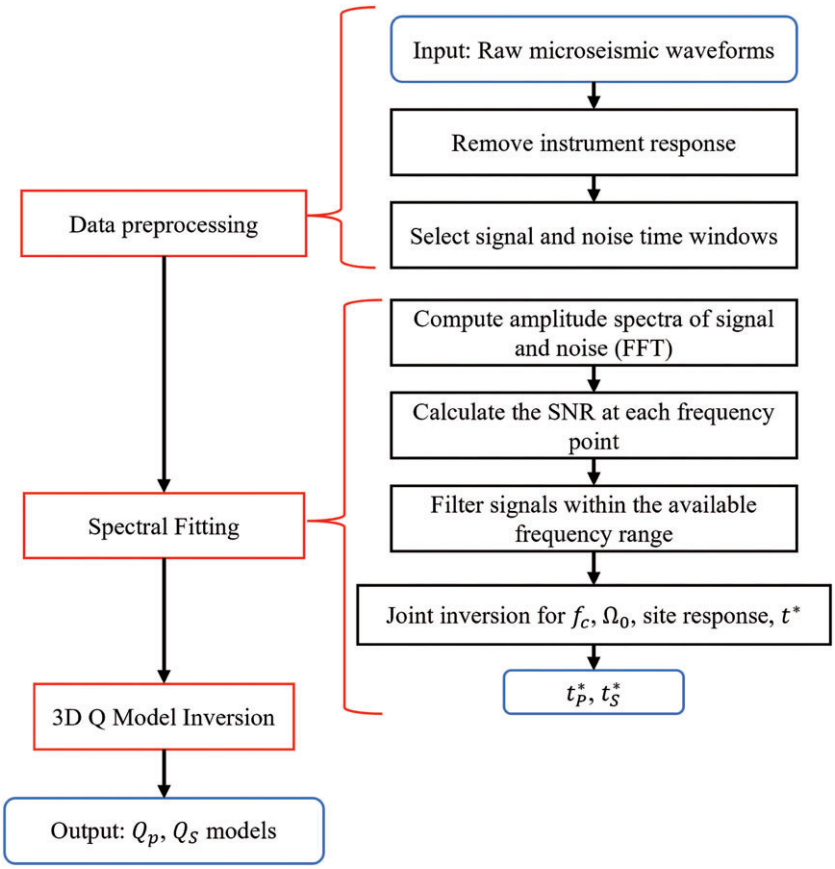

Figure 1. Flowchart of the adopted attenuation tomography method in this study.

tion term, respectively. These terms collectively influence the observed amplitude spectrum. The instrument response can be removed based on known instrument types. For the source term O_{ij}, the Brune source model can be used, and its expression in the far-field region is given by (Brune 1970):

$$O_{ij} = \frac{\Omega_{0_{ij}}}{1 + \left(f/\left(f_i^c\right)\right)^2}, \tag{2}$$

where $\Omega_{0_{ij}}$ represents the low-frequency amplitude term for event i and station j, which includes the influence of geometric spreading, f_i^c represents the corner frequency of earthquake event i, and f represents the frequency value. The path attenuation term B_{ij} can be expressed as

$$B_{ij} = e^{-\pi f\left(\frac{T_{ij}}{Q_{ij}}\right)} = e^{-\pi f t_{ij}^*}, \tag{3}$$

where T_{ij}, Q_{ij}, and t_{ij}^* represent the travel time, quality factor, and attenuation factor along the ray path, respectively. By removing the instrument response and taking the natural logarithm of both sides of Equation (1), the observed amplitude spectrum can be expressed as

$$\ln\left(A_{ij}^{corr}(f)\right) = \ln\left(\Omega_{0_{ij}}\right) - \ln\left(1 + \left(\frac{f}{f_i^c}\right)^2\right) + \ln\left(S_j(f)\right) - \pi f t_{ij}^*. \tag{4}$$

We can perform a joint inversion for all the observed amplitude spectra using Equation (4) to determine the unknown parameters (Bennington *et al.* 2008; Pesicek *et al.* 2011; Aster *et al.* 2018). The Levenberg-Marquardt method can enhance our ability to accurately invert the spectral data for model parameters (Marquardt 1963; Aster *et al.* 2018). The unknowns to be determined include the corner frequencies f_i^c for each event, the site effects $S_j(f)$ beneath each station, the low-frequency amplitude levels $\Omega_{0_{ij}}$ and attenuation factors t_{ij}^* for each station and each event.

We used a four-step alternating inversion scheme designed by Pesicek *et al.* (2011) that iteratively updates poorly constrained parameters while keeping other parameters fixed. In the first step, initial site effects beneath each station are determined based on an assumed value for t^*. During the iteration process, higher damping is applied to t^*, Ω_0, and f_c parameters to prioritize the update of the site effects. In the second step, a grid search is performed within a certain frequency range using the updated values of other parameters after the first step, aiming to find the best-fitting f_c for each event. The grid search approach helps to reduce the coupling between the corner frequency and t^* during the inversion process. In the third step, a direct linear inversion is applied to Ω_0 using the exponential form of Equation (4) after updating the other parameters. Finally, in the fourth step, the final iteration of the joint inversion is performed to determine the final t^* values. In this process, higher damping parameters are set for the other model parameters. Additionally, the joint inversion

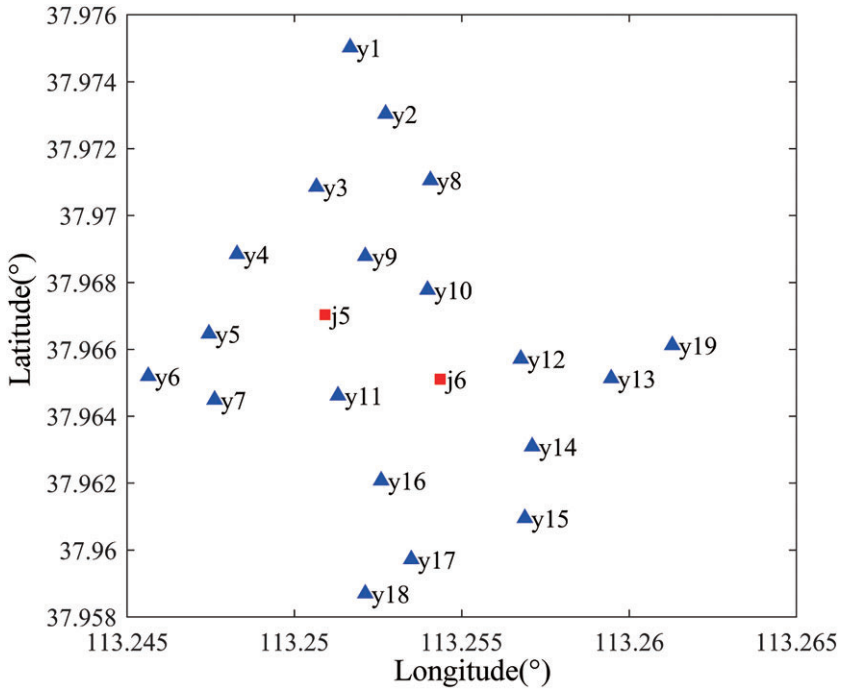

Figure 2. The plan view of surface geophones and two hydraulic fracturing well locations. The surface geophones are represented by blue triangles, and the hydraulic fracturing wells are represented by red squares.

is applied again instead of independently to update t^* values to ensure the best fitting between theoretic and observed amplitude spectra.

Lees & Lindley (1994) solved for a 3D Q model by summing frequency-dependent Q, i.e. $Q = Q_0 f^{\alpha}$. They found that even when ignoring frequency dependence, the Q model exhibits similar structures, and it is believed that frequency mainly influenced the absolute value of Q but not its spatial variations (Guo & Thurber 2021). Therefore, we assume that t^* values and Q are independent of frequency in the inversion.

2.2. Attenuation tomography method

After obtaining t^*, if we have already determined the velocity model and earthquake locations, we can invert for the Q model using the following relationship (Thurber & Eberhart-Phillips 1999):

$$t^* = \int_s \frac{1}{Q(x,y,z)} \frac{1}{V(x,y,z)} ds. \quad (5)$$

Based on the Equation (5), we can perform the inversion using the least-squares method by minimizing the misfit between observed and calculated t^* values, thereby obtaining the Q structure. For the attenuation tomography system, smoothing and damping are needed to regularize the inversion system, with optimal parameters selected by the trade-off analysis (Aster *et al.* 2018). The selected parameters ensure a balance between model length/smoothness and data fitting in the inversion process. Before the 3D inversion, we determine a homogenous Q value for the entire region that best fits all t^* values, which is called Qini and used as the initial Q model.

3. Data

In this study we use surface seismic monitoring data of two hydraulic fracturing wells (j5 and j6) in a coal mine located in Shanxi, China. The targeted coal seams are from the Taiyuan Formation in the Carboniferous system, located at depths ranging from 500 to 600 m below the surface. The average thickness of the coal seams is 3.33 m. A total of 19 geophones were deployed in the field within a 600-m radius centered around the wellhead, forming a circular microseismic monitoring network with geophones located along radii of 200, 400, and 600 m (Fig. 2). The average elevation of the stations is 1273.5 m above the mean sea level. These geophones were installed in shallow holes of 10 to 20 m deep to improve the signal to noise ratio of the data, with the sampling frequency of 1000 Hz. The hydraulic fracturing reservoir depth for well j5 ranges from 765 to 762 m above the mean sea level (MSL), while for well j6 it ranges from 735 to 733 m above the MSL (Fig. 3).

During the hydraulic fracturing process, a total of 346 microseismic events were detected. These events have magnitudes ranging from −1.0 to −2.0. The waveforms are characterized with weaker P-wave energy and relatively stronger S-wave energy. The waveform duration of the detected events is ∼4 seconds, with the main frequency falling within the range of 40–50 Hz.

4. Seismic attenuation analysis

In a previous study, Wang *et al.* (2023) has conducted seismic velocity tomography using these 346 events by the double-difference seismic tomography method (tomoDD; Zhang & Thurber 2003). The relocated microseismic events for two wells are spatially independent and overall have a north–south distribution in the horizontal directions with a vertical extent

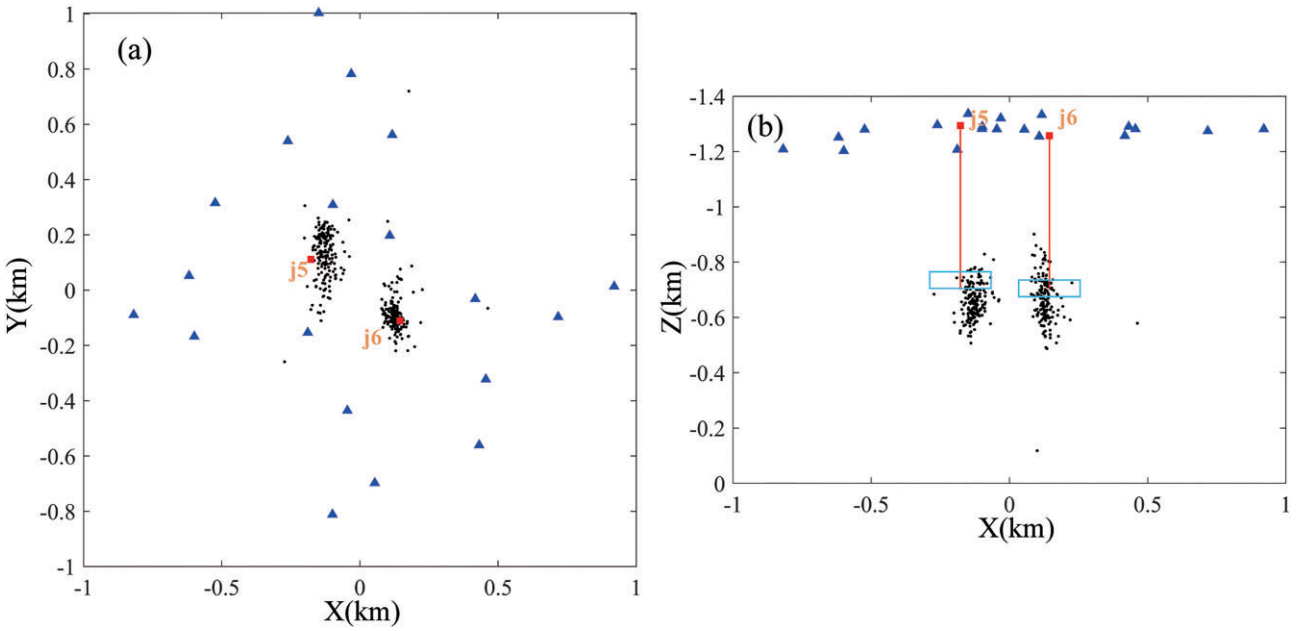

Figure 3. Earthquake locations using TomoDD. (a) Map view of the event locations. (b) Side view of the event locations. Stations are marked with blue triangles, and the wells are marked by red squares. Target reservoirs are marked with green rectangles.

exceeding 300 meters. For well j5, the microseismic events are primarily distributed on the eastern side of the fracturing well and below the fracturing zone. On the other hand, for well j6, the microseismic events are mainly distributed on the western side of the fracturing well. They extend both above and below the fracturing depth, with a greater extension below. The asymmetry in the microseismic event distribution may be attributed to deviations in the perforation locations (Maxwell *et al.* 2010) or variations in rock properties near the hydraulic fracturing well (Fisher & Warpinski 2012). In this study, we first calculate the t^* values for P- and S-waves using the respective waveforms. Subsequently, we conduct the attenuation tomography to determine the 3D Q_p and Q_s models.

First, we invert Ω_0, f_c, t^*, and site effects simultaneously using the amplitude spectra for all earthquakes observed at all stations (Bennington *et al.* 2008; Pesicek *et al.* 2011; Bisrat *et al.* 2014). We calculate the P- and S-wave amplitude spectra within a time window of 0.128 seconds covering the first-arrival P- and S-waves (0.02 seconds before and 0.108 seconds after the first arrival time) and the noise spectra within a time window of the same length preceding the P-wave arrival time. To avoid contamination from S-wave signals, only waveforms with S–P arrival time differences >0.13 s are used. We calculate the SNRs of amplitude spectra at each frequency between 20 and 500 Hz, and only those exceeding a threshold of 3 for at least 50 frequencies are selected.

The initial * values correspond to $Q_p = Q_s = 100$, based on experimental Q measurements (Murphy Iii 1982; Blakeslee *et al.* 1989; Chapman *et al.* 2006). The initial value for the site effect is set to 1, indicating no site effect. In Equation (5), the initial value of the corner frequency f_c, can be estimated using an empirical relationship for the corner frequency and the earthquake magnitude M_w, as follows (Chen & Bai 1991; Hu 2020):

$$\log_{10} f^c_{initial} = -0.333 \times M_w + 1.75. \quad (6)$$

The amplitude spectra fitting results are shown in Fig. 4, and the fitting value ("fit" in Fig. 4) is determined based on the root mean square (RMS) error of the spectral fitting process. The range from 0 (best) to 4 (worst) corresponds to a ranking system, where lower values indicate better agreement between the observed and calculated spectra. By exclusively selecting fitting values of 0, 1, and 2, we obtain a total of 5313 t^* values for P-waves and 5205 t^* values for S-waves. Most of these values are smaller than 0.015 s. Notably, the t^* values for S-waves are slightly larger than those for P-waves. Specifically, P-wave t* values are predominantly distributed between 0.005 and 0.01 s, while S-wave t^* values mainly fall within the range of 0.007 to 0.012 s (Fig. 5).

The distribution of corner frequency (f_c) with respect to magnitude (Mw) is shown in Fig. 6. The magnitude (Mw) is distributed within the range of −1 to −2, while the corner frequency (f_c) spans a wide range from 100 to 400 Hz. A clear linear relationship is observed between them with f_c increasing when Mw decreases, which is consistent with previous studies (Chen & Bai 1991; Allmann & Shearer 2009; Eisner *et al.* 2015; Hu 2020). According to the empirical formula relating f_c and stress drop ($\Delta\sigma$) (Eisner *et al.* 2015), microseismic events in this study have a stress drop ranging from 0.05 to 0.5 MPa, which is smaller than tectonic earthquakes. This could be due to the reduced normal stress by elevated pore fluid pressures on fault planes (Huang *et al.* 2017). The observed variations in stress drop may be influenced by variations in source geometry, rupture speed, and local velocity, as well as uncertainties in the corner frequency (Kaneko & Shearer 2014; Huang *et al.* 2017; Abercrombie 2021).

After obtaining the t^* values, we performed seismic attenuation tomography of Q_p and Q_s using the modified double-difference seismic tomographic system (Zhang & Thurber 2003; Bennington *et al.* 2008; Pesicek *et al.* 2011; Bisrat *et al.* 2014; Hu 2020; Guo & Thurber 2021). First, we determine homogeneous Q_p and Q_s values to serve as initial values for

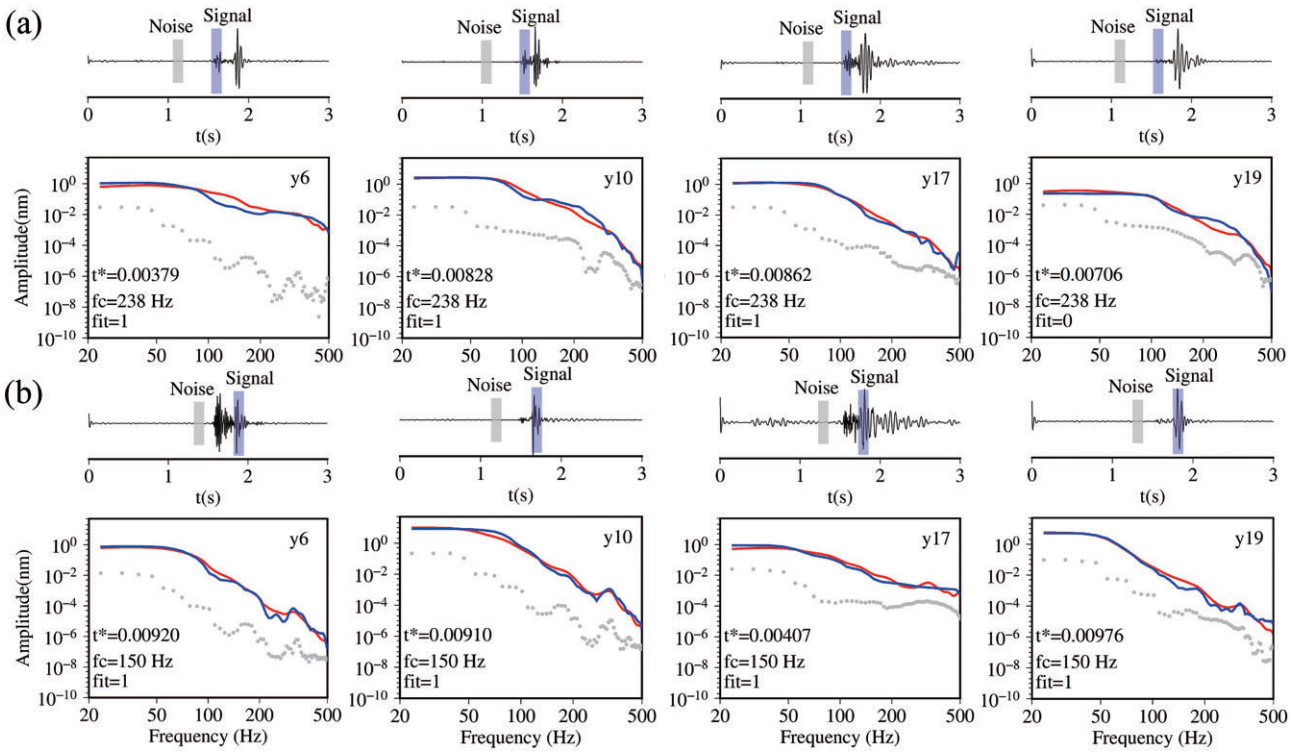

Figure 4. Examples of amplitude spectrum fitting for the (a) P-wave and (b) S-wave are presented for waveforms from a single event recorded at multiple stations. The upper panel displays the recorded waveforms for each station, with the P-wave shown as the vertical component (*Z* component) and the S-wave as the horizontal component (*N* component). The lower panel illustrates the results of the spectrum fitting. Here, the dark blue solid line represents the observed amplitude spectrum, the gray dashed line represents the noise spectrum, and the red solid line represents the calculated amplitude spectrum based on inversion results.

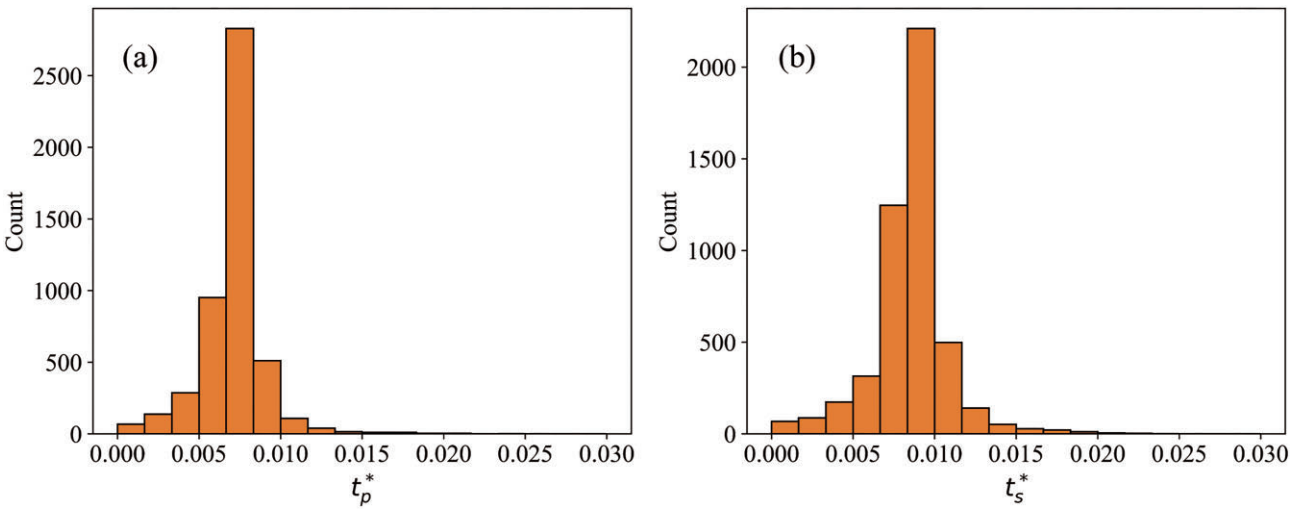

Figure 5. Histograms of estimated t^* values for (a) P-waves and (b) S-waves.

the inversion. We test a range of values from 0 to 150 in increments of 5 and find that $Q_P = 40$ and $Q_S = 50$ correspond to the minimum RMS residuals for $t_P{}^*$ and $t_S{}^*$, respectively (Fig. 7). These values were selected as they provide the best fit to the observed data, as demonstrated in Fig. 7.

For the 3D inversion, the coordinate system is chosen with the *x*-axis along the east–west direction and the *y*-axis along the north–south direction. Here we used a multi-grid inversion strategy by first setting a coarser inversion grid and then a finer inversion grid. For the coarser inversion grid, the grid spacing is set as 100 m in both the *x* and *y* directions within a range of −900 to 900 m, and in the depth direction, the grid nodes are set at $z = -1400, -1100, -800, -700, -600, -400$, and 0 m, where 0 m represents the MSL (positive downward). 10 and 12 iterations were performed separately for P- and S-waves and the final t^* residuals are mostly concentrated within 0.005 s with a Gaussian-like distribution (Fig. 8). For the finer inversion grid, the grid spacing is set as 50 m in both

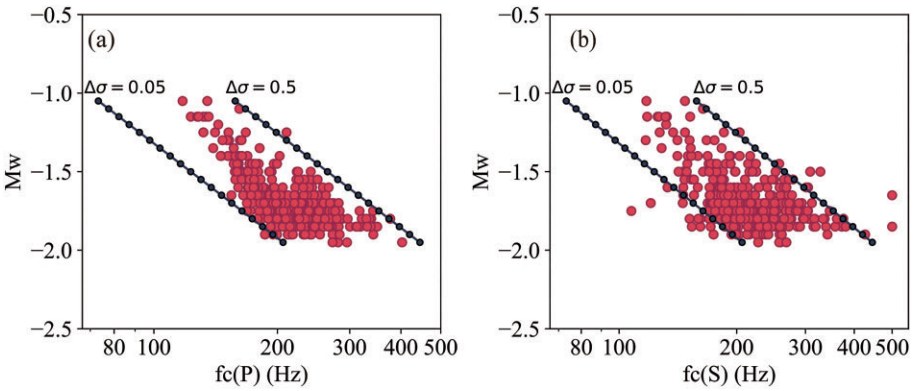

Figure 6. Statistical analysis of inverted corner frequencies for P- and S-waves. (a) Cross plot between inverted corner frequency f_c(P) and magnitude Mw. (b) Cross plot between inverted corner frequency f_c(S) and magnitude Mw. Lower bound of stress drop of 0.05 MPa and upper bound of stress drop of 0.5 MPa.

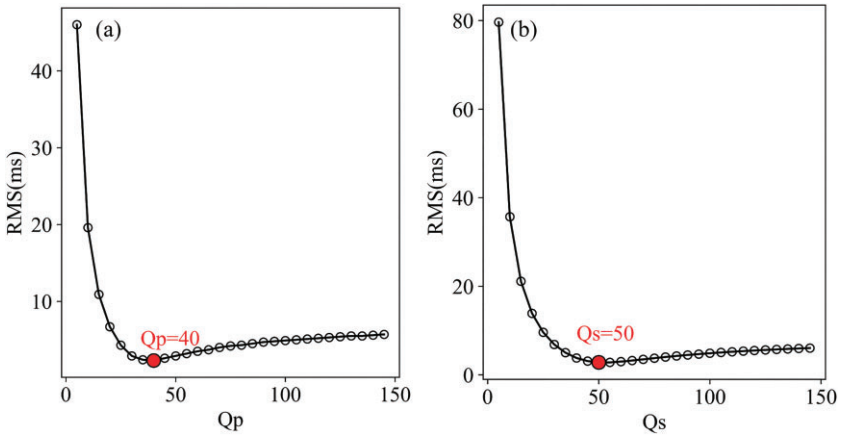

Figure 7. Selection for homogenous (a) Q_p and (b) Q_s values corresponding to the minimum RMS t^* residuals. The red dots indicate the chosen Q values.

x and y directions, and in the depth direction the grid nodes are finer with the grid spacing of 50 m in the depth range of −600 to −800 m. The initial Q_p and Q_s models for the finer inversion grid are the final inverted Q_p and Q_s models from the coarser grid inversion. The final RMS t_P* residual decreases from 0.00136 to 0.00109, and t_S* residual decreases from 0.00171 to 0.00138.

To assess the model resolutions for both coarser and finer inversion grids, we have conducted a conventional checkerboard test. In this test, a model with alternate positive and negative 5% anomalies were generated on the average Q model (Figs 9 and 10). It can be seen that the Q_p and Q_s models exhibit higher resolutions in the depth range of −600 to −800 m where the microseismicity is densely distributed. However, the resolution is relatively lower at shallower depths where the ray coverage is poorer. The checkerboard test shows that under the current data distribution both Q_p and Q_s anomalies with size between 50 and 100 m can be well resolved.

Vertical sections of 1000/Qp and 1000/Qs models from coarse-grid inversion are shown in Figure 11, respectively. Figures 12 and 13 show vertical profiles of the inverted Q_p and Q_s models with the finer inversion grid at $y = -0.1$, 0, and 0.1 km, using the coarse-grid results as the initial model (Fig. 11), and they are compared with V_p and V_s models along the same profiles. Similarly, we also show the inverted Q_p and Q_s models with the finer inversion grid at $x = -0.1$, 0, and 0.1 km, respectively (Fig. 14). For Q_p and Q_s models, although they are inverted separately, they still exhibit a high degree of similarity. Overall, microseismicity is associated with high Q_p and Q_s values. The two distinct microseismic clusters are nearly vertically aligned, and their spatial extension can be used to delineate fracturing zone geometry, as demonstrated by Wang *et al.* (2023). Both fracturing zones are primarily located within regions exhibiting low V_p, high V_s, and high Q_p and Q_s anomalies, with these anomalies aligning vertically as well. Additionally, low V_p, V_s, Q_p, and Q_s anomalies appear above the fracturing zones, indicating a significant transition in rock properties. This abrupt change in rock properties likely marks a boundary between different rock formations or fluid saturation states. Furthermore, the shallow low-velocity and low-Q anomalies extending toward the surface are suggested to correspond with unconsolidated near-surface sediments.

5. Discussion

In our study, by seismic attenuation tomography using inverted t^* values, we have determined Q_p and Q_s models for the target hydraulic fracturing reservoirs. It is clear that both Q_p and Q_s show high values around the fractured reservoirs (Figs. 12–14). In comparison, V_p shows low anomalies while V_s shows high anomalies (Figs. 12 and 13). It is known that by hydraulic fracturing, fractures will be created in the target reservoirs, which can be filled with fluids as well as extracted

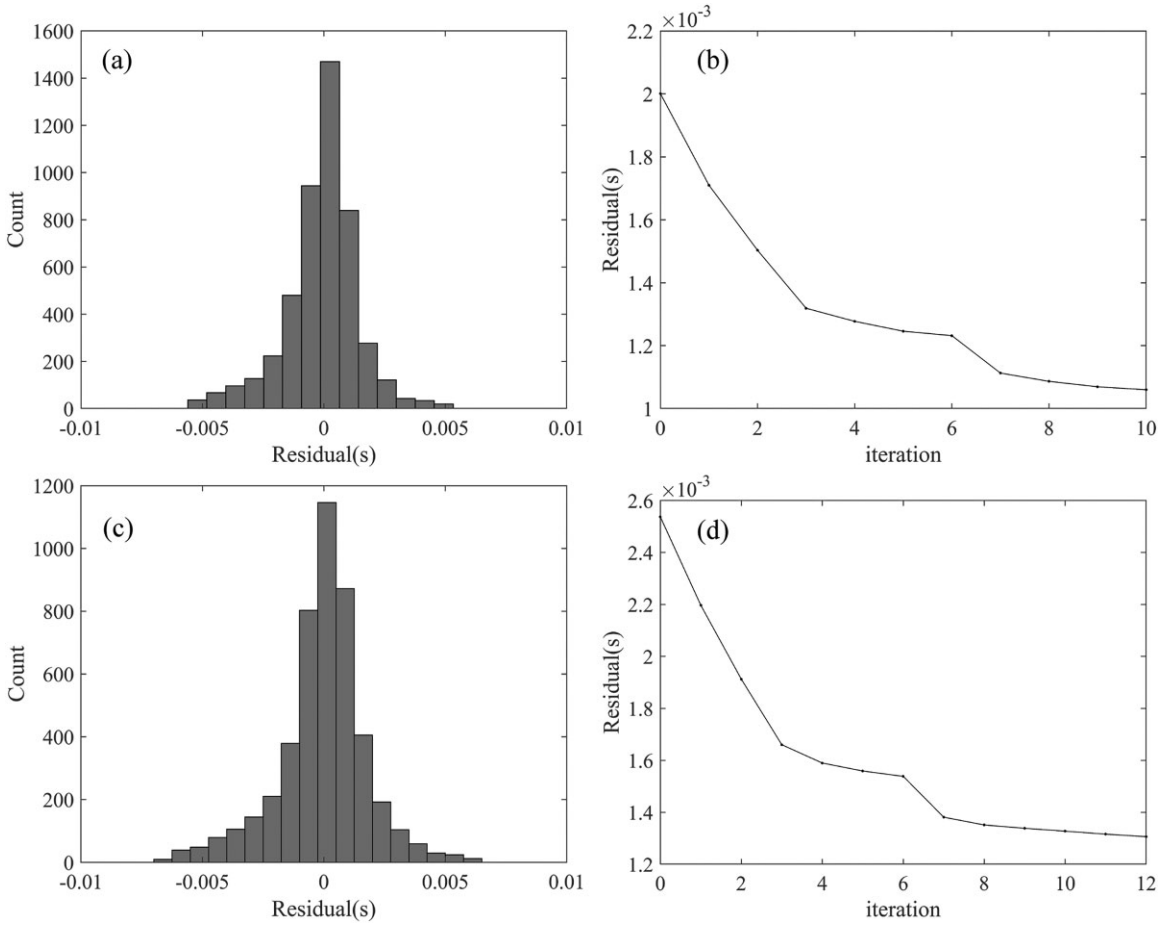

Figure 8. Distribution of final t^* residuals and RMS residuals with iterations for P- and S-waves with the coarser inversion grid. (a) Histogram of t^* residuals for P-wave after inversion. (b) Variation of RMS t^* residuals for P-wave with iterations. (c) Histogram of t^* residuals for S-wave after inversion. (d) Variation of RMS t^* residuals for S-wave with iterations.

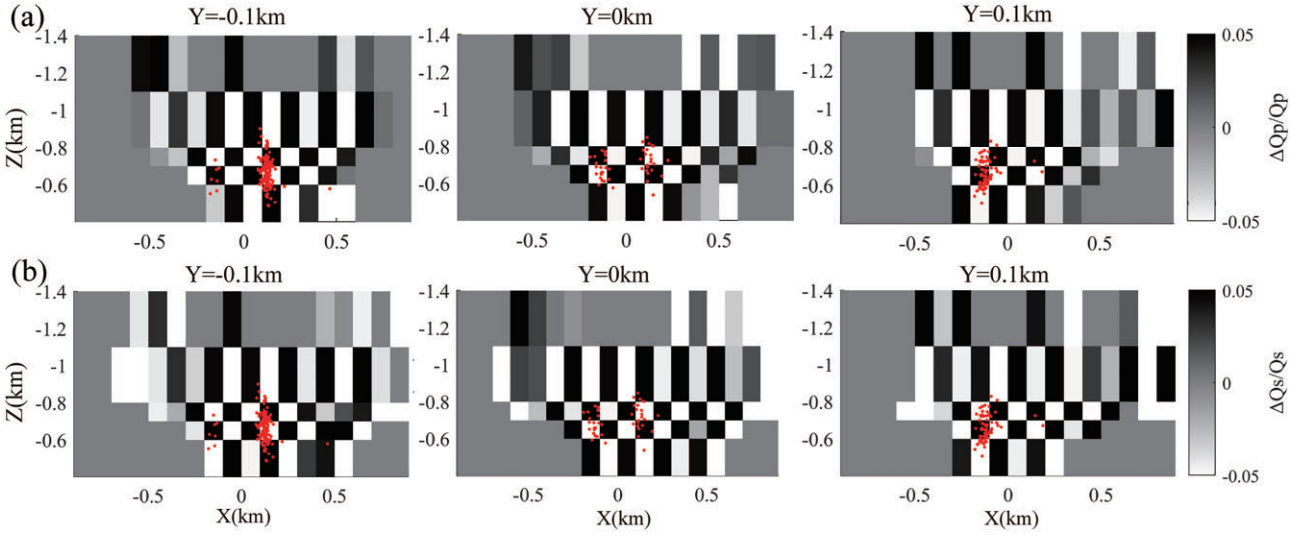

Figure 9. Recovered checkerboard patterns with a coarser inversion grid for (a) Q_p and (b) Q_s models along three profiles at $y = -0.1$, 0, and 0.1 km. Red dots denote seismic events within 50 m along the profile in the y-direction.

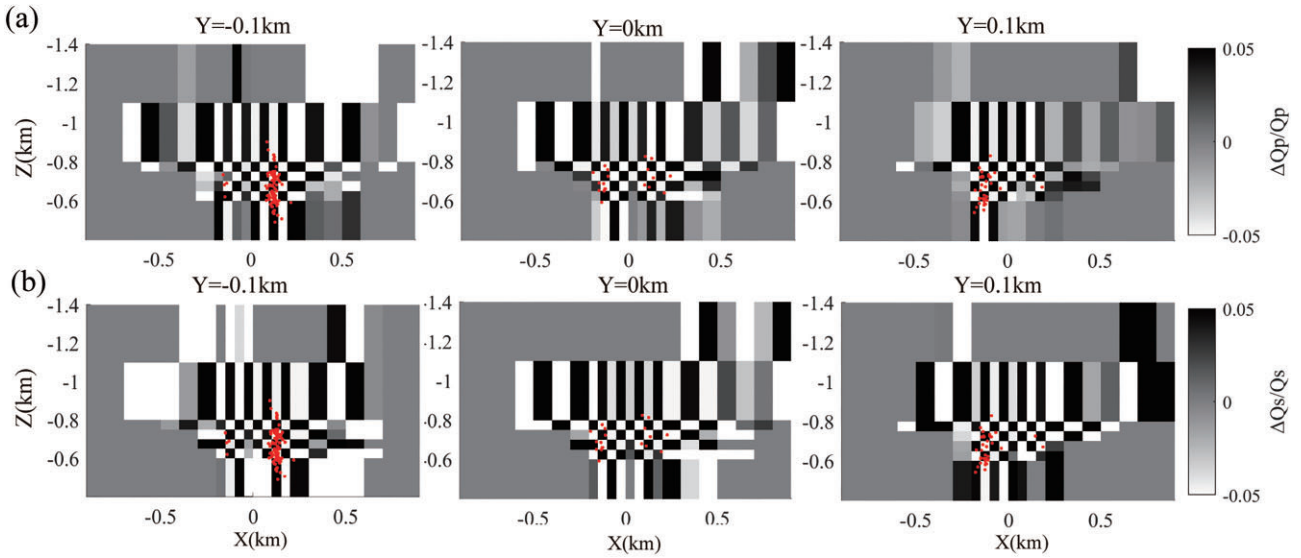

Figure 10. The same as Fig. 9 but for the finer inversion grid. Red dots denote seismic events within 25 m along the profile in the *y*-direction.

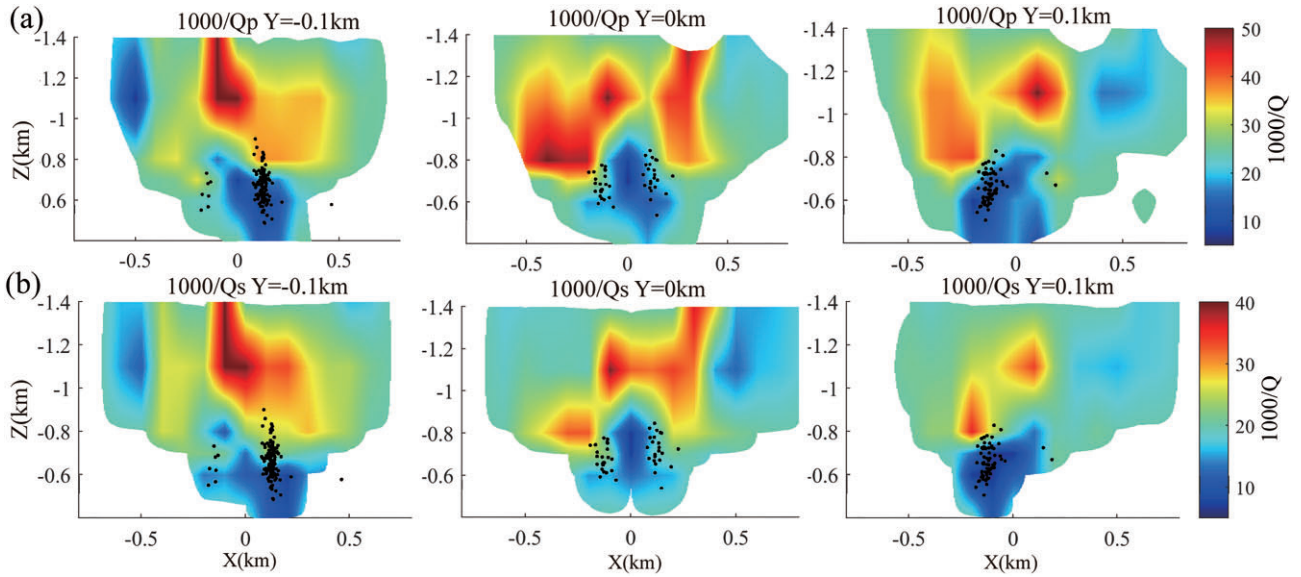

Figure 11. Vertical sections with a coarser inversion grid of (a) $1000/Q_p$ and (b) $1000/Q_s$ models at $y = -0.1$, 0, and 0.1 km. Black dots denote seismic events within 50 m along the profile in the *y*-direction.

coalbed methane. Therefore, the observed attenuation and velocity anomalies are affected by created fractures and filled fluids and gases.

Previous studies have indicated that the closure of microcracks with increasing effective stress can lead to a reduction in attenuation for P- and S-waves in both dry and saturated sedimentary and igneous rocks (Johnston *et al.* 1979; Johnston & Toksöz 1980). In comparison, when pores and induced fractures are partially or fully saturated with fluids, the propagating elastic waves can be attenuated (Liao *et al.* 2023). It is generally agreed that the dominant cause of attenuation in fluid-saturated porous rocks is the viscous fluid–solid interaction (Toksöz *et al.* 1979; Johnston & Toksöz 1980; Murphy Iii 1982). Numerical simulations by (Dutta & Odé 1979) on porous rocks under fluid saturation conditions demonstrated significant changes in acoustic properties and attenuation of elastic waves when a small amount of gas is present in brine-saturated rocks. The P-wave is mostly attenuated when gases are at an intermediate saturation state. Wu *et al.* (2014) proposed a two-layer model and analyzed the variation of P-wave attenuation with gas saturation under different porosities. The results indicate that attenuation is lowest when the gas is fully saturated and reaches its maximum at intermediate saturation levels. Liu *et al.* (2012) conducted ultrasonic testing on carbonate rocks with different gas saturation levels and found that longitudinal wave attenuation increases initially and then decreases with increasing gas saturation level, while transverse wave attenuation decreases linearly with increasing gas saturation level. Similar results have been reported in other laboratory measurements (Murphy Iii 1982; Wulff

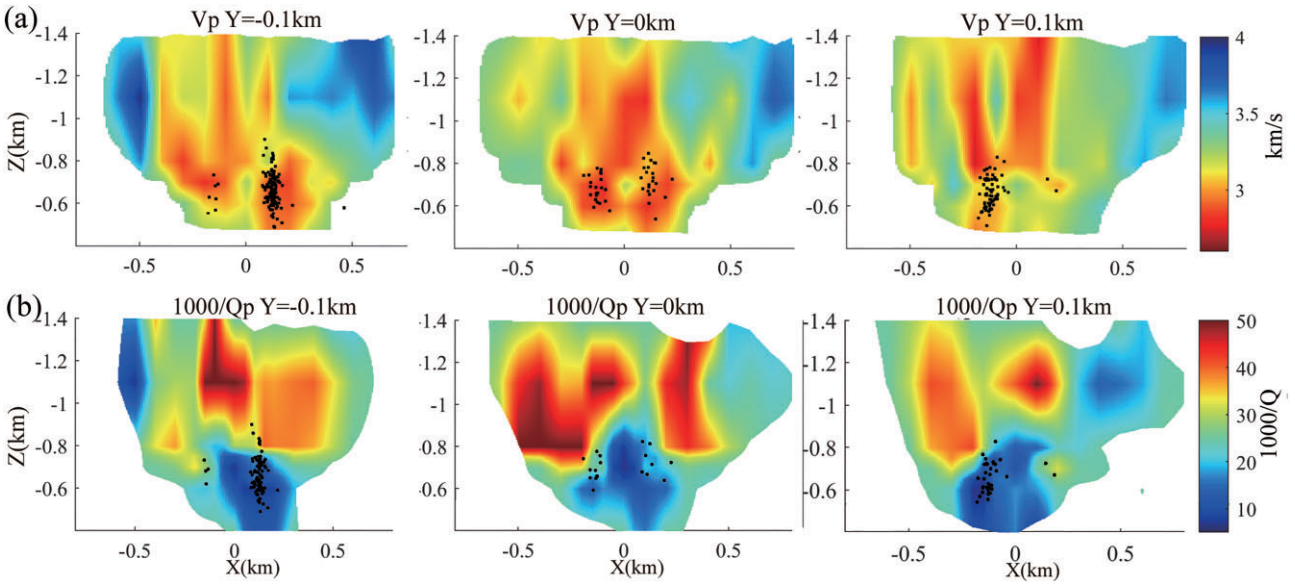

Figure 12. Vertical sections of (a) V_p and with a finer inversion grid of (b) $1000/Q_p$ models at $y = -0.1$, 0, and 0.1 km. Black dots denote seismic events within 25 m along the profile in the y-direction.

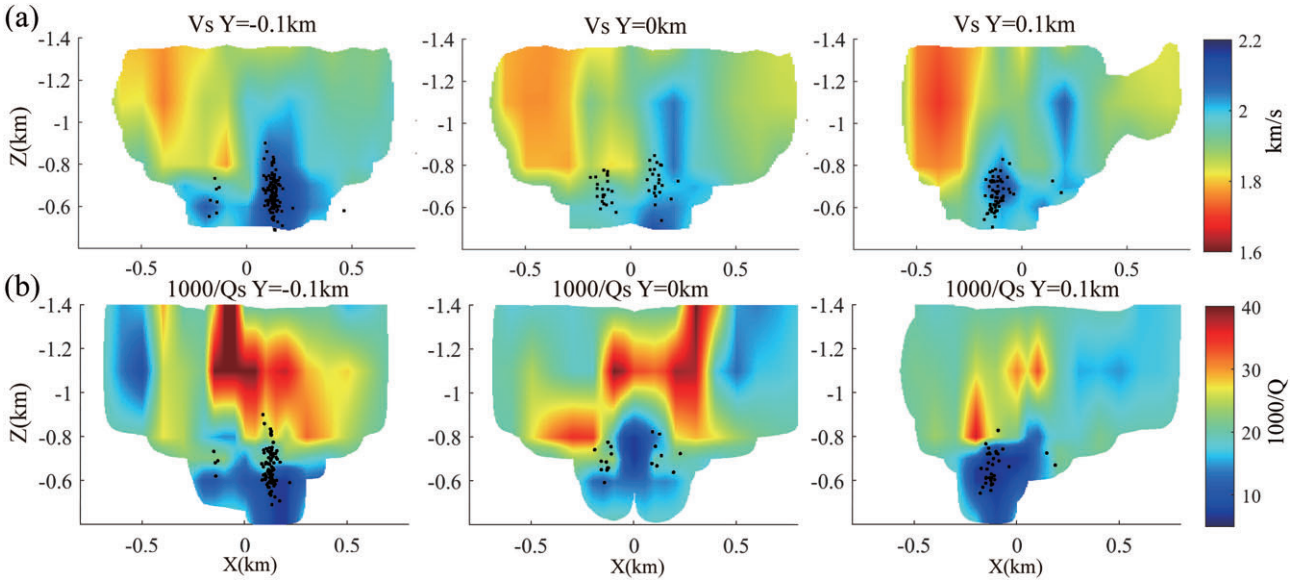

Figure 13. Vertical sections with a finer inversion grid of (a) V_s and (b) $1000/Q_s$ models at $y = -0.1$, 0, and 0.1 km. Black dots denote seismic events within 25 m along the profile in the y-direction.

& Burkhardt 1997; Amalokwu *et al.* 2014; Caspari *et al.* 2014).

Therefore, the imaged high Q_p and Q_s values, or lower attenuation in and around target reservoirs are most likely caused by gas saturated fractures. However, the central portion of the Q_p and Q_s models ($y = 0$) corresponds to an area with fewer recorded microseismic events, suggesting less-fractured zones. This phenomenon may indicate lower gas saturation near the edges of the fracturing zones and lower Q compared to the zones with microseismic events along profiles at $y = 0.1$ and $y = -0.1$ km. The existence of high Q values in the fractured zones suggests that intrinsic attenuation reduction, most likely due to gas saturation, outweighs scattering losses. Furthermore, at $x = 0$ km in the $y = 0$ km profiles, the absence of microseismicity aligns with high velocity anomalies and high Q_p and Q_s values. This implies structurally intact, less-fractured rock formations within the central zone, likely unaffected by hydraulic stimulation. Thus, we can use high Q (low attenuation) anomalies to characterize the gas saturation zones caused by hydraulic fracturing, which are located in the range of $x, y = -0.2$ to 0.2 km and $z = -0.4$ to -0.8 km. The presence of fractures and fluids typically results in a reduction in both V_p and V_s. However, for gas-filled fractures, they induce a significant V_p reduction due to the abrupt drop in bulk modulus. In contrast, V_s exhibits a distinct behavior: the shear modulus (μ) remains largely unaffected by the gas inclusion

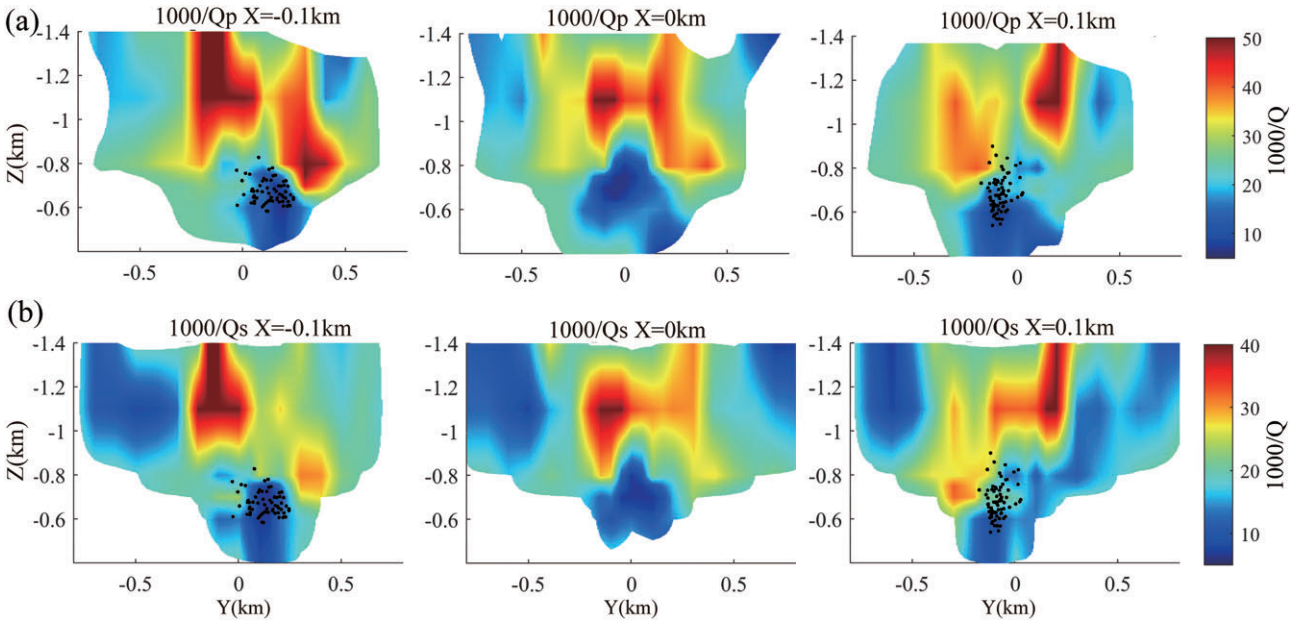

Figure 14. Vertical sections with a finer inversion grid of (a) $1000/Q_p$ and (b) $1000/Q_s$ models at $x = -0.1$, 0, and 0.1 km. Black dots denote seismic events within 25 m along the profile in the x-direction.

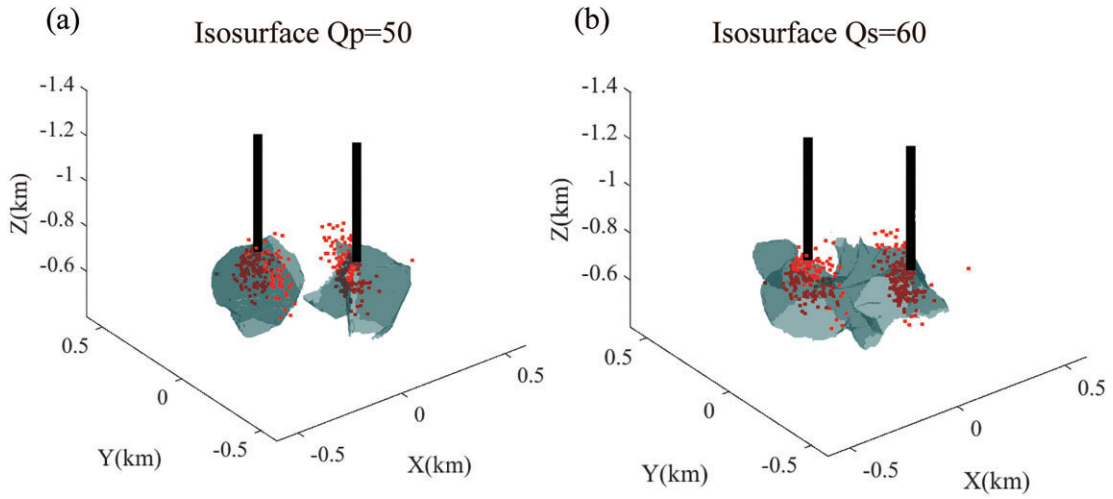

Figure 15. The distribution of high Q anomalies near the fractured reservoirs delineating effective fracturing zones. (a) $Q_p = 50$ isosurface. (b) $Q_s = 60$ isosurface. In each figure, the two black lines delineate the two hydraulic fracturing wells. The blue regions depict the isosurfaces of $Q_p = 50$ and $Q_s = 60$ with low V_p (<3 km/s), highlighting areas of low seismic attenuation, while the red dots illustrate microseismic events.

while the density decreases, leading to an increase in V_s and a reduction in the V_p/V_s ratio (Toksöz *et al.* 1976). High Q_p and Q_s zones are consistent with observed low V_p and high V_s anomalies, which are caused by high gas saturation levels.

In the attenuation model, above −0.8 km there are relatively high attenuation anomalies extended to the surface and widely distributed horizontally (low Q_p and Q_s values; Figs 12–14), which may be attributed to loosely consolidated sediments in the shallow region. Based on the widespread low-velocity and low-Q anomalies down to a depth of $z = -1.0$ km, the thickness of the sedimentary layer can be estimated to be ∼400 m.

For hydraulic fracturing, it is important to characterize the fractured zones to assess the future production potential of reservoirs. In general, the volume covered by microseismic events induced by hydraulic fracturing is used for this purpose. However, the effective fracturing stimulation volume estimated solely based seismicity distribution could be biased (Zimmer 2011). As seen in Figs 12 and 13, high Q_p and Q_s zones around the target reservoirs, which could be treated as a proxy for effective stimulation reservoir volume, are not consistent with the microseismicity distribution. For example, in the Q_p and Q_s vertical sections along $y = 0.1$ km, there is little seismicity within high Q_p and Q_s zones to the right of $x = 0$ (Figs 12 and 13). Therefore, we can use attenuation anomalies to better delineate fracturing zones by extracting high Q_p ($Q_p = 50$) and high Q_s ($Q_s = 60$) isosurfaces (Fig. 15). Considering that intact or unfractured rock formations also show high Q values, here we combine the V_p model to create high Q_p and Q_s isosurfaces delineating fracturing zones. For gas

saturation zones, the associated V_p values are low. Therefore, only high Q_p and Q_s zones with low V_p values represent effective fracturing zones with high gas content. We see from Fig. 15 that the high Q anomalies extend outward from the bottom of the two fracturing wells into the surrounding areas. Notably, the seismic events are predominantly located within the high Q anomaly zones. This spatial correlation suggests that the fractures are saturated with gases, indicating the release of a large amount of CBM from target reservoirs.

The microseismic attenuation tomography method used in this study can also be applied to assess the fracture distribution for other unconventional oil/gas resources such as shale gas, tight oil, and hot dry rock system developed by hydraulic fracturing (e.g. Aki *et al.* 1982; Adam *et al.* 2009; De Siena *et al.* 2010; Li *et al.* 2016). However, this method has some limitations. If microseismic monitoring stations are not well distributed, the attenuation model resolutions may be poor, especially in the region where the ray path coverage is sparse. In addition, the inverted Q models may also consist of scattering attenuation, and coda wave analysis is need to separate it from the intrinsic attenuation (Aki & Chouet 1975).

6. Conclusions

By using t^* values inverted from seismic waveforms from microseismic events induced by coalbed methane hydraulic fracturing, we have determined 3D Q_p and Q_s models for the target coal beds by the attenuation tomography. Seismic attenuation Q_p and Q_s models exhibit a high degree of similarity. Around the target coal reservoirs, both Q_p and Q_s exhibit pronounced high values, which are interpreted due to high gas saturation based on previous rock physics experiments. These high Q values are associated with low V_p and high V_s anomalies, consistent with the scenario of gas saturated fractures. Overall, high Q_p, high Q_s, low V_p, and high V_s zones around the fractured coalbed reservoirs are consistent, which are caused by high saturation of coalbed methane in the fractures created by hydraulic fracturing. The results suggest that these models are reliable and can be used to assess the effective stimulated reservoir volume.

Acknowledgements

We are grateful for the field crew from Wantai Geophysical Technology Co. Ltd for data collection and initial data analysis.

Conflict of interest statement

None declared.

Funding

This research is funded by National Key R&D Program of China (grant no. 2022YFF0800701).

Data availability

Microseismic waveforms used in this study can be accessed via https://github.com/JiachenWang20749/Microseismic-Waveforms.

References

Abercrombie RE. 2021. Resolution and uncertainties in estimates of earthquake stress drop and energy release. *Philos Trans A Math Phys Eng Sci*, **379**:20200131. https://doi.org/10.1098/rsta.2020.0131

Adam L, Batzle M, Lewallen KT, Van Wijk K. 2009. Seismic wave attenuation in carbonates. *J Geophys Res Solid Earth*, **114**:B06208. https://doi.org/10.1029/2008JB005890

Aki K, Chouet B. 1975. Origin of coda waves: source, attenuation, and scattering effects. *J Geophys Res*, **80**:3322–42. https://doi.org/10.1029/JB080i023p03322

Aki K, Fehler M, Aamodt R, Albright J, Potter R, Pearson C, Tester J. 1982. Interpretation of seismic data from hydraulic fracturing experiments at the Fenton Hill, New Mexico, hot dry rock geothermal site. *J Geophys Res*, **87**:936–44. https://doi.org/10.1029/JB087iB02p00936

Al-Damegh K, Sandvol E, Al-Lazki A, Barazangi M. 2004. Regional seismic wave propagation (Lg and Sn) and Pn attenuation in the Arabian Plate and surrounding regions. *Geophys J Int*, **157**:775–95. https://doi.org/10.1111/j.1365-246X.2004.02246.x

Alexandrov D, Eisner L, Waheed UB, Kaka SI, Greenhalgh SA. 2020. Detection, location, and source mechanism determination with large noise variations in surface microseismic monitoring. *Geophysics*, **85**:KS197–206. https://doi.org/10.1190/geo2019-0841.1

Allmann BP, Shearer PM. 2009. Global variations of stress drop for moderate to large earthquakes. *J Geophys Res-Sol Ea*, **114**:B01310. https://doi.org/10.1029/2008JB005821

Amalokwu K, Best AI, Sothcott J, Chapman M, Minshull T, Li X-Y. 2014. Water saturation effects on elastic wave attenuation in porous rocks with aligned fractures. *Geophys J Int*, **197**:943–7. https://doi.org/10.1093/gji/ggu076

Aster RC, Borchers B, Thurber CH. 2018. *Parameter Estimation and Inverse Problems*. 3rd edn. Amsterdam, Netherlands: Elsevier.

Barthwal H, Calixto FJ, Van Der Baan M. 2019. 3-D attenuation tomography from microseismicity in a mine. *Geophys J Int*, **219**:1805–17. https://doi.org/10.1093/gji/ggz396

Bennington N, Thurber C, Roecker S. 2008. Three-dimensional seismic attenuation structure around the SAFOD site, Parkfield, California. *Bull Seismol Soc Am*, **98**:2934–47. https://doi.org/10.1785/0120080175.

Bisrat ST, Deshon HR, Pesicek J, Thurber C. 2014. High-resolution 3-DP wave attenuation structure of the New Madrid Seismic Zone using local earthquake tomography. *J Geophys Res Solid Earth*, **119**:409–24. https://doi.org/10.1002/2013JB010555

Blake OO, Faulkner DR, Bascombe R. 2020. Using the Q factor to detect closed microfractures. *Geophysics*, **85**:MR285–95. https://doi.org/10.1190/geo2019-0093.1

Blakeslee S, Malin P, Alvarez M. 1989. Fault-zone attenuation of high-frequency seismic waves. *Geophys Res Lett*, **16**:1321–4. https://doi.org/10.1029/GL016i011p01321

Bowden DC, Tsai VC, Lin FC. 2017. Amplification and attenuation across USArray using ambient noise wavefront tracking. *J Geophys Res Solid Earth*, **122**:10086–101. https://doi.org/10.1002/2017JB014804

Brune JN. 1970. Tectonic stress and the spectra of seismic shear waves from earthquakes. *J Geophys Res*, **75**:4997–5009. https://doi.org/10.1029/JB075i026p04997

Campillo M, Bouchon M, Massinon B. 1984. Theoretical study of the excitation, spectral characteristics, and geometrical attenuation of regional seismic phases. *Bull Seismol Soc Am*, **74**:79–90. https://doi.org/10.1785/BSSA0740010079

Caspari E, Qi Q, Lopes S, Lebedev M, Gurevich B, Rubino JG, Velis DR *et al.* 2014. Wave attenuation in partially saturated porous rocks—new observations and interpretations across scales. *Leading Edge*, **33**:606–14. https://doi.org/10.1190/tle33060606.1

Chambers K, Kendall JM, Brandsberg-Dahl S, Rueda J. 2010. Testing the ability of surface arrays to monitor microseismic activity. *Geophys Prospect*, **58**:821–30. https://doi.org/10.1111/j.1365-2478.2010.00893.x

Chapman M, Liu E, Li X-Y. 2006. The influence of fluid sensitive dispersion and attenuation on AVO analysis. *Geophys J Int*, **167**:89–105. https://doi.org/10.1111/j.1365-246X.2006.02919.x

Chen P, Bai T. 1991. Quantification relations between the source parameters. *Acta Seismol Sin*, **13**:401–11 (in Chinese)

Chen Y, Zhang H, Miao Y, Zhang Y, Liu Q. 2017. Back azimuth constrained double-difference seismic location and tomography for downhole microseismic monitoring. *Phys Earth Planet Inter*, **264**:35–46. https://doi.org/10.1016/j.pepi.2016.10.003

Dalton CA, Ekström G. 2006. Global models of surface wave attenuation. *J Geophys Res*, **111**:B05317. https://doi.org/10.1029/2005JB003997

De Siena L, Del Pezzo E, Bianco F. 2010. Seismic attenuation imaging of Campi Flegrei: evidence of gas reservoirs, hydrothermal basins, and feeding systems. *J Geophys Res Solid Earth*, **115**:B09307. https://doi.org/10.1029/2009JB006938

Dutta N, Odé H. 1979. Attenuation and dispersion of compressional waves in fluid-filled porous rocks with partial gas saturation (White model)—Part II: results. *Geophysics*, **44**:1789–805. https://doi.org/10.1190/1.1440939

Eisner L, Gei D, Hallo M, Oprsal I, Ali M. 2015. The peak frequency of direct waves for microseismic events. *Geophysics*, **78**:A45–9. https://doi.org/10.1190/geo2013-0197.1

Ellsworth WL. 2013. Injection-induced earthquakes. *Science*, **341**:142. https://doi.org/10.1126/science.1225942

Fisher K, Warpinski N. 2012. Hydraulic-fracture-height growth: real data. *SPE Prod Oper*, **27**:8–19. https://doi.org/10.2118/145949-PA

Frankel A. 1991. Mechanisms of seismic attenuation in the crust: scattering and anelasticity in New York State, South Africa, and southern California. *J Geophys Res Solid Earth*, **96**:6269–89. https://doi.org/10.1029/91JB00192

Guo H, Thurber C. 2021. Double-difference seismic attenuation tomography method and its application to The Geysers geothermal field, California. *Geophys J Int*, **225**:926–49. https://doi.org/10.1093/gji/ggab017

Han W, Wang Y, Li Y, Ni X, Wu X, Wu P, Zhao S. 2021. Recognizing fracture distribution within the coalbed methane reservoir and its implication for hydraulic fracturing: a method combining field observation, well logging, and micro-seismic detection. *J Nat Gas Sci Eng*, **92**:103986. https://doi.org/10.1016/j.jngse.2021.103986

Hu J. 2020. *Development of regional-scale seismic velocity and attenuation tomography methods and its applications. Ph.D. Thesis*. Hefei: University of Science and Technology of China. (in Chinese).

Huang Y, Ellsworth WL, Beroza GC. 2017. Stress drops of induced and tectonic earthquakes in the central United States are indistinguishable. *Science Adv*, **3**:e1700772.

Jiang T, Zhang J, Wu H. 2016. Experimental and numerical study on hydraulic fracture propagation in coalbed methane reservoir. *J Nat Gas Sci Eng*, **35**:455–67. https://doi.org/10.1016/j.jngse.2016.08.077

Johnston DH, Toksöz MN. 1980. Ultrasonic P and S wave attenuation in dry and saturated rocks under pressure. *J Geophys Res Solid Earth*, **85**:925–36. https://doi.org/10.1029/JB085iB02p00925

Johnston DH, Toksöz MN, Timur A. 1979. Attenuation of seismic waves in dry and saturated rocks: II. Mechanisms. *Geophysics*, **44**:691–711. https://doi.org/10.1190/1.1440970

Kaneko Y, Shearer PM. 2014. Variability of seismic source spectra, estimated stress drop, and radiated energy, derived from cohesive-zone models of symmetrical and asymmetrical circular and elliptical ruptures. *J Geophys Res Solid Earth*, **120**:1053–79. https://doi.org/10.1002/2014JB011642

Karaoğlu H, Romanowicz B. 2017. Global seismic attenuation imaging using full-waveform inversion: a comparative assessment of different choices of misfit functionals. *Geophys J Int*, **212**:807–26. https://doi.org/10.1093/gji/ggx442

Knopoff L. 1964. *Q*. *Rev Geophys*, **2**:625–60. https://doi.org/10.1029/RG002i004p00625

Lawrence JF, Prieto GA. 2011. Attenuation tomography of the western United States from ambient seismic noise. *J Geophys Res Solid Earth*, **116**:B06302. https://doi.org/10.1029/2010JB007836

Lawrence JF, Shearer PM, Masters G. 2006. Mapping attenuation beneath North America using waveform cross-correlation and cluster analysis. *Geophys Res Lett*, **33**:L07315. https://doi.org/10.1029/2006GL025813

Lees JM, Lindley GT. 1994. Three-dimensional attenuation tomography at Loma Prieta: inversion of *t** for Q. *J Geophys Res Solid Earth*, **99**:6843–63. https://doi.org/10.1029/93JB03460

Li F, Verma S, Zhou H, Zhao T, Marfurt KJ. 2016. Seismic attenuation attributes with applications on conventional and unconventional reservoirs. *Interpretation*, **4**:SB63–77 https://doi.org/10.1190/INT-2015-0105.1.

Liao J, Wen P, Guo J, Zhou L. 2023. Seismic dispersion, attenuation and frequency-dependent anisotropy in a fluid-saturated porous periodically layered medium. *Geophys J Int*, **234**:331–45. https://doi.org/10.1093/gji/ggad080

Lin F-C, Tsai VC, Ritzwoller MH. 2012. The local amplification of surface waves: a new observable to constrain elastic velocities, density, and anelastic attenuation. *J Geophys Res Solid Earth*, **117**:B09302. https://doi.org/10.1029/2012JB009208

Liu X, Wang S, Liu H, Zhu H, Chen Q, Long Y. 2012. Experimental test on the effects of carbonate gas saturation on ultrasonic wave attenuation characteristics. *Oil Geophys Prospect*, **47**:926–30 (in Chinese).

Mao Q, Azeem T, Zhong Y, Wang P, Gui Z, Zhou S. 2025. A downhole migration-based location method based on cross-correlation-weighted semblance for microseismic events. *J Geophys Eng*, **22**:697–708. https://doi.org/10.1093/jge/gxaf033

Marquardt DW. 1963. An algorithm for least-squares estimation of nonlinear parameters. *J. Soc. Ind. Appl. Math*, **11**:431–41. https://doi.org/10.1137/0111030

Maxwell S. 2014. Microseismic imaging of hydraulic fracturing: improved engineering of unconventional shale reservoirs. pp. 214, Tucson, USA: Society of Exploration Geophysicists. https://doi.org/10.1190/1.9781560803164

Maxwell SC, Rutledge J, Jones R, Fehler M. 2010. Petroleum reservoir characterization using downhole microseismic monitoring. *Geophysics*, **75**:75A129–37. https://doi.org/10.1190/1.3477966

Miao S, Zhang H, Chen Y, Tan Y, Miao Y, Huang Z, Wang F *et al.* 2019. Surface microseismic monitoring of shale gas hydraulic fracturing based on microseismic location and tomography. *Geophys Prospect Petrol*, **58**:262–71 (in Chinese).

Mohamed T, Mehana M. 2020. Coalbed methane characterization and modeling: review and outlook. *Energy Sources Part A*, **47**:2874–96. https://doi.org/10.1080/15567036.2020.1845877

Moore TA. 2012. Coalbed methane: a review. *Int J Coal Geol*, **101**:36–81. https://doi.org/10.1016/j.coal.2012.05.011

Murphy Iii WF. 1982. Effects of partial water saturation on attenuation in Massilon sandstone and Vycor porous glass. *J Acoust Soc Am*, **71**:1458–68. https://doi.org/10.1121/1.387843

Nicolas M, Massinon B, Mechler P, Bouchon M. 1982. Attenuation of regional phases in Western Europe. *Bull Seismol Soc Am*, **72**:2089–106. https://doi.org/10.1785/BSSA07206A2089

Peacock S, Mccann C, Sothcott J, Astin TR. 1994. Experimental measurements of seismic attenuation in microfractured sedimentary rock. *Geophysics*, **59**:1342–51. https://doi.org/10.1190/1.1443693

Pesicek J, Bennington N, Thurber C, Zhang H. 2011. Improving attenuation tomography by novel inversions for *t** and *Q*: application to Parkfield, California and Okmok volcano, Alaska. *AGU Fall Meeting*. Available at: http://www.geology.wisc.edu/homepages/to_be_removed/pesicek/public_html/download/pesicek_AGU11v2.pdf (30 July 2025, date last accessed).

Pozgay SH, Wiens DA, Conder JA, Shiobara H, Sugioka H. 2009. Seismic attenuation tomography of the Mariana subduction system: implications for thermal structure, volatile distribution, and slow spreading dynamics. *Geochem Geophys Geosyst*, **10**:Q04X05. https://doi.org/10.1029/2008GC002313

Romero AE, Jr, Mcevilly TV, Majer EL. 1997. 3-D microearthquake attenuation tomography at the Northwest Geysers geothermal region, California. *Geophysics*, **62**:149–67. https://doi.org/10.1190/1.1444114

Scherbaum F. 1990. Combined inversion for the three-dimensional Q structure and source parameters using microearthquake spectra. *J Geophys Res Solid Earth*, **95**:12423–38. https://doi.org/10.1029/jb095ib08p12423

Thurber C, Eberhart-Phillips D. 1999. Local earthquake tomography with flexible gridding. *Comput Geosci*, **25**:809–18. https://doi.org/10.1016/S0098-3004(99)00007-2

Toksöz M, Johnston DH, Timur A. 1979. Attenuation of seismic waves in dry and saturated rocks: I. Laboratory measurements. *Geophysics*, **44**:681–90. https://doi.org/10.1190/1.1440969

Toksöz MN, Cheng C, Timur A. 1976. Velocities of seismic waves in porous rocks. *Geophysics*, **41**:621–45. https://doi.org/10.1190/1.1440639

Tromp J, Tape C, Liu Q. 2005. Seismic tomography, adjoint methods, time reversal and banana-doughnut kernels. *Geophys J Int*, **160**:195–216. https://doi.org/10.1111/j.1365-246X.2004.02453.x

Wang J, Zhang H, Zhao L, Zha H, Cheng T, Shi X, Liu J *et al.* 2023. Evaluation of the coalbed methane hydraulic fracturing effect based on microseismic event locations and tomography results for surface microseismic monitoring. *Geophys Prospect Petrol*, **62**:31–42+55 (in Chinese). https://doi.org/10.3969/j.issn.1000-1441.2023.01.002

Wang T, Liu X, Liu L, Tang J, Zhang X, Cao F. 2024. Impact hazard analysis of islanding face mining based on micro-seismic monitoring and shock wave CT inversion. *J Geophys Eng*, **22**:520–31. https://doi.org/10.1093/jge/gxae130

Wang YH. 2012. Reservoir characterization based on seismic spectral variations. *Geophysics*, **77**:M89–95. https://doi.org/10.1190/geo2011-0323.1

Wu X, Chapman M, Li XY, Boston P. 2014. Quantitative gas saturation estimation by frequency-dependent amplitude-versus-offset analysis. *Geophys Prospect*, **62**:1224–37. https://doi.org/10.1111/1365-2478.12179

Wulff AM, Burkhardt H. 1997. Dependence of seismic wave attenuations and velocities in rock on pore fluid properties. *Phys Chem Earth*, **22**:69–73. https://doi.org/10.1016/S0079-1946(97)00080-3

Yang X, Lin Z, Yang X, Chen Z, Si W. 2023. Micro-seismic monitoring using sparse planar array and a weak signal enhancement method. *J Geophys Eng*, **20**:965–77. https://doi.org/10.1093/jge/gxad060

Zhang H, Thurber CH. 2003. Double-difference tomography: the method and its application to the Hayward Fault, California. *Bull Seismol Soc Am*, **93**:1875–89. https://doi.org/10.1785/0120020190

Zhao L-F, Mousavi SM. 2018. Lateral variation of crustal Lg attenuation in eastern North America. *Sci Rep*, **8**:7285. https://doi.org/10.1038/s41598-018-25649-5

Zhu H, Bozdağ E, Duffy TS, Tromp J. 2013. Seismic attenuation beneath Europe and the North Atlantic: implications for water in the mantle. *Earth Planet Sci Lett*, **381**:1–11. https://doi.org/10.1016/j.epsl.2013.08.030

Zimmer U. 2011. Calculating stimulated reservoir volume (SRV) with consideration of uncertainties in microseismic event locations. In: *Canadian Unconventional Resources Conference*. SPE International (United States). https://doi.org/10.2118/148610-MS

Received: December 15, 2024; Revised: June 3, 2025; Accepted: June 28, 2025